# Co$_3$O$_4$ quantum dots/TiO$_2$ nanobelt hybrids for highly efficient photocatalytic overall water splitting

Jie Liu[a,1], Jun Ke[b,1], Ying Li[a], Baojun Liu[c], Lidong Wang[a,*], Huining Xiao[a], Shaobin Wang[d,*]

[a] Department of Environmental Science & Engineering, North China Electric Power University, Baoding, 071003, China
[b] School of Chemistry and Environmental Engineering, Wuhan Institute of Technology, Wuhan, 430073, China
[c] College of Resource and Environmental Engineering, Guizhou University, Guiyang, 550025, China
[d] Department of Chemical Engineering, Curtin University, GPO Box U1987, Perth, WA, 6845, Australia

## ARTICLE INFO

## ABSTRACT

Solar-light driven water splitting to hydrogen and oxygen without sacrificial agents has gained tremendous attention due to the clean and renewable energy supply of the future. Herein, we report construction of Co$_3$O$_4$ quantum dots (QDs)/TiO$_2$ nanobelts (NBs) hybrids via a facile hydrothermal method for simultaneous H$_2$ and O$_2$ productions from pure water, with high evolution rates of 41.8 and 22.0 $\mu$mol h$^{-1}$ g$^{-1}$, respectively, which are significantly enhanced compared with TiO$_2$ NBs and Co$_3$O$_4$ materials. The Co$_3$O$_4$ QDs not only improve light sensitivity but also change the work function of TiO$_2$, promoting the transfer of electrons from TiO$_2$ to Co$_3$O$_4$ QDs and H$_2$ generation on the surface of Co$_3$O$_4$ QDs. Moreover, the size effect of Co$_3$O$_4$ QDs ($\sim$3 nm) facilitates the electron trapping due to the shorter pathway, and the generation of heterojunctions favors to suppress the recombination of photo-excited carries.

## 1. Introduction

Solar-light driven water splitting is a promising strategy for clean hydrogen production from water, which represents the most universally abundant and renewable energy carrier [1–3]. Overall water splitting contains two half reactions, hydrogen evolution (HE) and oxygen evolution (OE), and the OE reaction is considered as the rate-determining reaction due to the coupling of more electrons and the transfer of more protons [4–6]. Up to date, numerous semiconductor materials, including TiO$_2$, CdS, Bi$_2$O$_3$, Co$_3$O$_4$, WO$_3$, and g-C$_3$N$_4$, etc, act as the photocatalysts for the two half reactions [7–11], whereas developing an efficient and stable photocatalyst to accomplish the overall water splitting without using sacrificial agents, noble metals and external bias, is still a challenge [12,13].

With a suitable band structure, TiO$_2$ is regarded as the benchmark material in photocatalytic reactions, and it makes HE reaction thermodynamically possible. Whereas the low light utilization efficiency due to the wide band gap ($E_g = \sim$3.2 eV for anatase) and rapid recombination of photogenerated electron–hole pairs inhibits its further application [14–17]. It was found that the engineered heterojunctions in photocatalysts could be a promising solution to improve the activity of catalysts by facilitating the spatial separation of photogenerated

electron-hole pairs [18–20]. For the fabrication of TiO$_2$-based hybrids used for water splitting, Co$_3$O$_4$ is an appropriate candidate due to its narrow band gap of $\sim$2.1 eV and excellent oxidation ability, which are confirmed to benefit the water oxidation [21,22]. According to Yu's work, the activity of TiO$_2$-based materials for photocatalytic H$_2$ generation could be greatly enhanced by co-deposition of Co$_3$O$_4$ and Pt, and the co-decoration of Co$_3$O$_4$ and Pt is also effective for nitrogen-doped TiO$_2$, which reported by Cui et al. [23,24]. For the cobalt decoration, Maeda et al. also suggested that the activity of photocatalytic water splitting strongly depends on the distribution of Co$_3$O$_4$ nanoclusters, which was proved by a rutile titania-based catalyst loaded with cobalt oxide nanoclusters [25]. Compared with bulk materials, 0-dimensional (0D) quantum dots (QDs) of Co$_3$O$_4$ have attracted more attention. The small size of QDs ($<$ 10 nm) leads to a larger specific surface area to provide more active sites, and the shorter charger transport paths and the quantum confinement of QDs also favor the photocatalytic reactions [26–28]. For a hybrid photocatalyst decorated by QDs, the construction of heterojunctions also helps to suppressing self-aggregation of QDs and increasing the dispersion and stability of QDs [29,30]. Recently, a Co$_3$O$_4$ QDs/g-C$_3$N$_4$ hybrid was reported for improved photocatalytic OE reaction [31], and a family of vanadate QDs on g-C$_3$N$_4$ also exhibited superior visible-light-driven

---

photocatalytic performance [32].

Herein we develop a new $Co_3O_4$ QDs/$TiO_2$ nanobelt (0D/2D) system by a facile hydrothermal method, which exhibits the excellent performances in the HE and OE half reactions as well as overall water splitting without sacrificial agents and noble metals under simulated solar light. The loading of $Co_3O_4$ QDs changes the work function of $TiO_2$, leading to a strong electron transfer from $TiO_2$ to $Co_3O_4$ QDs spontaneously and accumulation on the surface of $Co_3O_4$ QDs to participate in the reaction of HE. The size effect of $Co_3O_4$ QDs also facilitates the electron capture. Meanwhile, the heterojunctions formed between $Co_3O_4$ QDs and $TiO_2$ suppress the recombination of photoexcited electron-hole pairs. The as-prepared $Co_3O_4$ QDs/$TiO_2$ hybrids provide a promising opportunity for further development of solar water splitting based on $TiO_2$ nanomaterials.

## 2. Experimental

### 2.1. Synthesis of photocatalysts

#### 2.1.1. Synthesis of $TiO_2$ nanobelts (NBs)

Commercial P25 (0.8 g) was immersed in 60 mL of 10 M NaOH solution and ultrasonically treated for 30 min, which was then transferred to a Teflon-lined autoclave (100 mL) and reacted at 180 °C for 24 h. The obtained slurry was washed by 0.1 M HCl solution until the pH value decreased to ∼ 2, followed by washing with de-ionized (DI) water and ethanol, and dried at 60 °C for 12 h. Finally, the obtained precursor was annealed at 500 °C in air for 4 h at a heating rate of 4 °C min$^{-1}$ to obtain $TiO_2$ NBs.

#### 2.1.2. Synthesis of $Co_3O_4$ QDs/$TiO_2$ NBs

For the fabrication of $Co_3O_4$ QDs/$TiO_2$ NBs, 0.4 g $TiO_2$ NBs, 0.9 g urea and certain amount of $Co(NO_3)_2$·$6H_2O$ were dissolved in a mixture of DI water (30 mL) and ethanol (30 mL), and ultrasonicated for 30 min. The suspension was transferred to a Teflon-lined autoclave (100 mL) and reacted at 180 °C for 10 h. The obtained slurry was washed by DI water and ethanol, dried at 60 °C for 12 h, and calcined at 500 °C for 4 h at a heating rate of 4 °C·min$^{-1}$ to obtain a $Co_3O_4$ QDs/$TiO_2$ NBs hybrid. A series of $Co_3O_4$ QDs/$TiO_2$ samples were obtained at the $Co_3O_4$/$TiO_2$ molar ratios of 0.02, 0.04 and 0.06, and denoted as $Co_3O_4$/$TiO_2$-*x*, where *x* represents the molar ratio of $Co_3O_4$/$TiO_2$. For comparison, a pure $Co_3O_4$ material was prepared by the similar method without adding of $TiO_2$ NBs.

### 2.2. Characterizations

X-ray diffraction (XRD) was carried out on a Bruker D8-Advanced X-ray instrument using Cu K$\alpha$ radiation ($\lambda$ = 1.5418 Å). Raman analysis was performed on an ISA dispersive Raman spectroscope using argon ion laser with a wavelength at 532 nm. The morphology of the as-prepared materials was observed by a transmission electron microscope (TEM, FEI-Tecnai G$^2$ F20 S-TWIN) and a high-resolution transmission electron microscope (HR-TEM, FEI-Tecnai G$^2$ F20 S-TWIN). UV–vis diffuse reflection spectroscopy (DRS) was carried out on an UV–vis spectrophotometer (JASCOV-670) with a wavelength range of 250–800 nm. The photoluminescence (PL) spectra were obtained at room temperature in the spectral range of 350–750 nm using a Xe-lamp laser with a wavelength of 325 nm as the excitation source. X-ray photoelectron spectroscopy (XPS) and valence band XPS (VB-XPS) of various samples were carried out on a Kratos AXIS Ultra DLD system under ultrahigh vacuum (UHV) conditions with a base pressure less than $1 \times 10^{-9}$ mb, and the binding energies of C 1 s, Co 2p, Ti 3d and O 1 s were calibrated using C 1 s (BE = 284.8 eV) as a standard. Ultraviolet photoemission spectroscopy (UPS) experiments were recorded using the He I line at $h\nu$ = 21.22 eV as the excitation source, and the Fermi level position was calibrated using a gold reference (work function of 5.0 eV). The work function ($\Phi$) of catalyst samples was

determined according to the equation of $\Phi = h\nu - (E_{Fermi} - E_{cutoff})$, where $E_{Fermi}$ and $E_{cutoff}$ represent the energies of the Fermi edge and secondary electron cutoff, respectively.

### 2.3. Photoelectrochemical (PEC) tests

The PEC measurements were carried out using a Chi 660e electrochemical workstation operated in a standard three-electrode cell with a fluorine-doped tin oxide (FTO) electrode deposited with the as-prepared catalysts as a photoanode, a saturated calomel electrode (SCE) as the reference electrode and a Pt wire as the counter electrode. For the fabrication of the working electrode, 40 mg of a catalyst was mixed with a certain amount of ethanol and Nafion solution homogeneously, and the obtained sample was deposited as a thin film on the FTO glass with a controlled area of 1 cm$^2$ using spin-coating, and then dried at 60 °C for 30 min to form a film electrode. The PEC performance of the catalysts was measured under a 300 W Xe-lamp, and 0.5 M $Na_2SO_4$ solution (40 mL, pH = 6.8, 25 °C). The electrochemical impedance spectroscopy (EIS) was carried out in the frequency range of $10^{-1} \sim 10^5$ Hz.

### 2.4. Photocatalytic water splitting measurements

The performance of the as-prepared catalysts for the photocatalytic water splitting was measured by the half reactions of water splitting ($H_2$ and $O_2$ evolutions) and overall water splitting, which were carried out under a simulated solar irradiation by a 300 W Xenon lamp (CEL-PE300L-3 A, cut by 1.5 A M filter) and a constant reaction temperature of 25 °C. The $H_2$ and $O_2$ yields were analyzed by a gas chromatograph (GC, Agilent 7890 II) with a TCD detector. For the photocatalytic $H_2$ generation, 50 mg catalyst was well-dispersed in a mixture of 50 mL $H_2O$ and 5 mL methanol after sonication for 30 min, and 1.0 wt.% Pt nanoparticles were loaded on the sample as cocatalysts, which were rooted in $H_2PtCl_6$ by an *in-situ* photodeposition method. For the photocatalytic $O_2$ evolution, 50 mg of catalyst was added to 100 mL of solution including $AgNO_3$ (0.03 M) and $La_2O_3$ (0.1 g). Before irradiation, the suspensions were mixed under vigorous stirring for 30 min in dark and degassed to remove $O_2$ in solution. For the photocatalytic overall water splitting, 50 mg of catalyst was well-dispersed in 100 mL of DI water without any sacrificial agent or noble metal. Prior to the recycling tests of the overall water splitting, the used catalyst was collected by filtration, washed, and dried at 100 °C for 12 h, and the reactor was degassed at 100 °C for 4 h in vacuum.

## 3. Results and discussion

### 3.1. Characterizations of catalysts

XRD patterns of as-prepared photocatalysts are displayed in Fig. 1. $TiO_2$ NBs show high crystallinity and mixed crystals of anatase and rutile $TiO_2$ (PDF #21-1272 and # 65-0190). The main crystal phase is anatase $TiO_2$, and the peaks with weak intensities at 27.4, 36.0 and 62.7° are assigned to the (110), (101) and (002) planes of rutile $TiO_2$, respectively. The diffraction peaks of the as-prepared bulk cobalt oxide match well with a cubic phase of $Co_3O_4$ (PDF #34-1003). The XRD patterns of various $Co_3O_4$ QDs/$TiO_2$ samples are similar to that of $TiO_2$ NBs without peaks of $Co_3O_4$ species. It is worth noting that the main diffraction peak of $TiO_2$ NBs, centered at 25.3° and attributed to the (101) plane of anatase $TiO_2$, has a blue shift after the deposition of $Co_3O_4$ QDs, suggesting the strong interaction between the $Co_3O_4$ QDs and $TiO_2$ support and successful construction of $Co_3O_4$ QDs/$TiO_2$ heterojunctions [33]. Furthermore, the Raman spectra of catalysts are displayed in Fig. 1b. The as-prepared $TiO_2$ NBs show the Raman lines at around 145, 197, 399, 517 and 639 cm$^{-1}$, corresponding to the $E_g^1$, $E_g^2$, $B_{1g}^1$, $B_{1g}^2$ and $E_{g3}$ modes of anatase $TiO_2$, respectively [33,34]. The peaks of Raman shifts at 195, 484, 524, 620 and 691 cm$^{-1}$ on the pure $Co_3O_4$

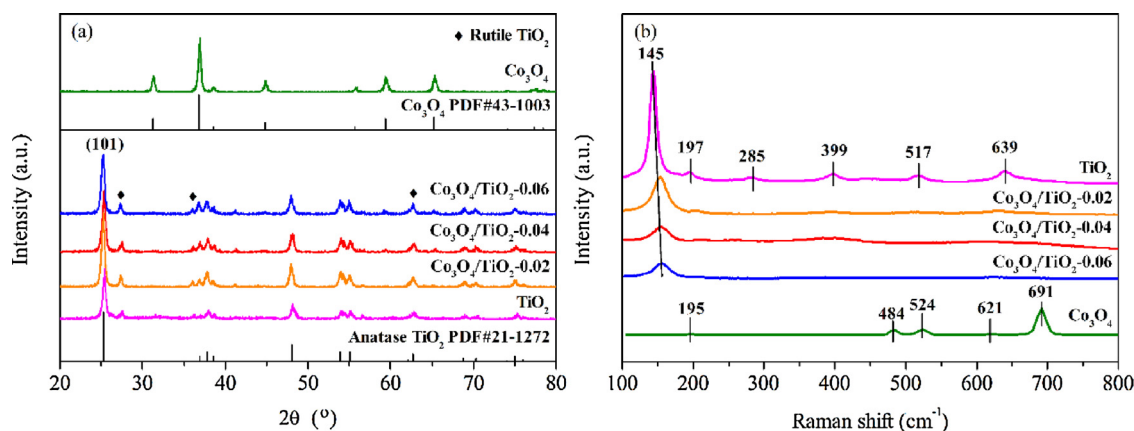Fig. 1. XRD patterns (a) and Raman spectra (b) of the as-prepared TiO$_2$ NBs, Co$_3$O$_4$ and various Co$_3$O$_4$ QDs/TiO$_2$ hybrids.

sample correspond to the $E_{2g}^1$, $E_{2g}^2$, $E_{2g}^3$, $F_g^{22}$ and A$_{1g}$ Raman-active modes of the cubic phase Co$_3$O$_4$, respectively [35,36]. For the Co$_3$O$_4$ QDs/TiO$_2$ samples, only the feature peak of anatase TiO$_2$ is observed at ~145 cm$^{-1}$, which shifts to the higher wavenumber with the increasing Co$_3$O$_4$ concentration, and the significantly decreased intensity. The Raman results are agreement with that from XRD patterns, confirming the interaction between Co$_3$O$_4$ QDs and TiO$_2$ NBs and the finely dispersion of Co$_3$O$_4$ QDs on TiO$_2$ NBs.

Fig. 2 displays SEM and TEM images of the as-prepared TiO$_2$ NBs and Co$_3$O$_4$ QDs/TiO$_2$ NBs samples. From Fig. 2a and b, the TiO$_2$ support shows well-defined morphology in nanobelts, with the width of ~50 nm, and the interplane distance of 0.218 nm matches well with the

(111) plane of rutile TiO$_2$ (Fig. 2c). The Co$_3$O$_4$/TiO$_2$-0.04 shows the similar morphology to TiO$_2$ NBs (Fig. 2d), interpreting that no obvious agglomeration occurs during the introduction of Co$_3$O$_4$ species. From Fig. 2e, the loaded Co$_3$O$_4$ exists as QDs, finely dispersed on the surface of TiO$_2$ NBs with an approximately diameter of 3 nm, and the homogeneous distribution is further confirmed by the elemental mapping of a selected nanobelt of Co$_3$O$_4$/TiO$_2$-0.04 sample (Fig. 2g). The $d$ spacings of 0.202 and 0.218 nm in Fig. 2f are assigned to the (400) plane of Co$_3$O$_4$ and the (111) plane of rutile TiO$_2$, respectively. The co-existence of Co$_3$O$_4$ and TiO$_2$ suggests the high possibility for the formation of a heterojunction, which may serve as migration paths to facilitate the transfer of photo-generated electrons and holes and inhibit the
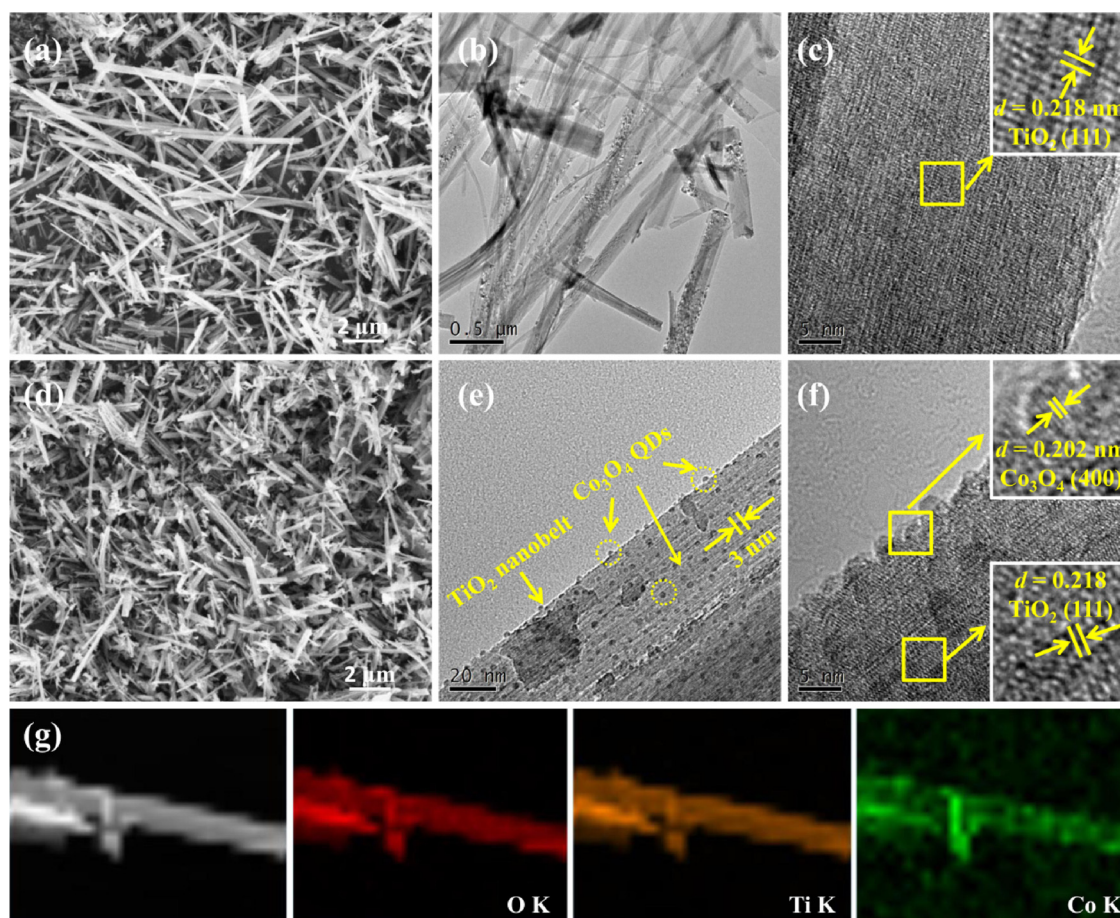


Fig. 2. SEM, TEM and HRTEM images of TiO$_2$ NBs (a, b, c) and Co$_3$O$_4$/TiO$_2$-0.04 (d, e, f) samples, and the elemental mapping of Co$_3$O$_4$/TiO$_2$-0.04 (g).
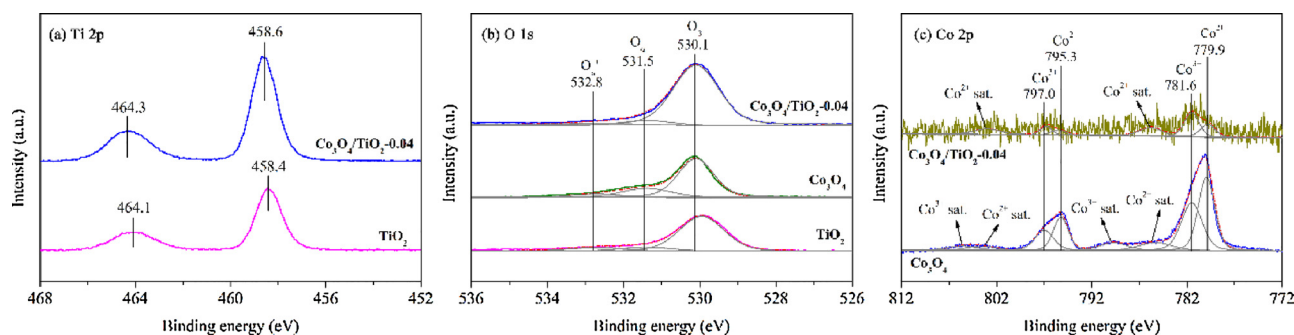
**Fig. 3.** XPS spectra of Ti 3d (a), O 1 s (b) and Co 2p (c) of the as-prepared $TiO_2$ NBs, $Co_3O_4$ and $Co_3O_4/TiO_2$-0.04 samples.

recombination of the charge carries [37,38]. The SEM, TEM and HRTEM images of the as-prepared pure $Co_3O_4$ material are displayed in Fig. S1 in Supporting Information, which exhibits a plate-shaped morphology assembled by nanoparticles, and the $d$ spacing of 0.285 nm is assigned to the (220) plane of $Co_3O_4$.

The as-prepared catalysts were further characterized by XPS to identify the surface chemical compositions and valence states (Fig. 3). For the Ti 2p XPS spectrum of $TiO_2$ NBs, the characteristic doublets of $Ti^{4+}$ centered at 464.1 and 458.4 eV are assigned to Ti $2p_{1/2}$ and Ti $2p_{3/2}$, respectively [39], while the feature peaks of $Ti^{4+}$ on $Co_3O_4/$ $TiO_2$-0.04 hybrid shift to a higher binding energy by 0.2 eV, interpreting the strong interaction between $Co_3O_4$ QDs and $TiO_2$ support. Fig. 3b presents the O 1 s XPS spectra of the catalysts, in which the fitted peaks centered at 530.1, 531.5 and 532.8 eV are attributed to the lattice oxygen ($O_\beta$), surface adsorbed oxygen ($O_\alpha$) mainly derived from oxygen vacancies, and chemisorbed water ($O_\alpha$'), respectively [20,40]. Fig. 3c displays the high resolution XPS spectra of Co 2p of samples. For the pure $Co_3O_4$, the main peaks at 795.3 and 779.9 eV are assigned to the Co $2p_{1/2}$ and Co $2p_{3/2}$ spin-orbital photoelectrons, respectively. The Co 2p profile of $Co_3O_4$ is fitted into eight species, including two pairs of spin–orbit doublets for the coexistence of $Co^{2+}$ and $Co^{3+}$ and their four shakeup satellites (denoted as "sat") [21,41]. By comparison, the main peaks of Co $2p_{1/2}$ and Co $2p_{3/2}$ on $Co_3O_4/TiO_2$-0.04 shift to the higher binding energy, which could be caused by the increase of $Co^{3+}$ species, and the presence of $Co^{2+}$ species could be proved by the spin-orbital splitting between the Co $2p_{3/2}$ and Co $2p_{1/2}$ peaks of 15.4 eV, as well as the satellite peaks of $Co^{2+}$. From Fig. 3c, the valence state distribution of Co species on $Co_3O_4/TiO_2$-0.04 is different from that of $Co_3O_4$, which could be caused by the interaction between $Co_3O_4$ QDs and $TiO_2$ NB support.

### 3.2. Performance of photocatalytic water splitting

The activities of catalysts for the half reactions of water splitting, photocatalytic hydrogen and oxygen evolution reactions, have been measured under the simulated solar illumination conditions. For the photocatalytic $H_2$ generation reaction (Fig. 4a and b), the average rate of $H_2$ generation on $TiO_2$ NBs is 1363.1 µmol $h^{-1}$ $g^{-1}$, while the pure $Co_3O_4$ shows a limited activity with the average rate of 29.3 µmol $h^{-1}$ $g^{-1}$. By comparison, the decoration of $Co_3O_4$ QDs on $TiO_2$ NBs with an appropriate loading favors the photocatalytic $H_2$ production. The average rate of $H_2$ generation on $Co_3O_4/TiO_2$-0.04 is increased to 1735.1 µmol $h^{-1}$ $g^{-1}$, whereas $Co_3O_4/TiO_2$-0.02 and $Co_3O_4/TiO_2$-0.06 samples exhibit the reduced activity, with the $H_2$ generation rates at 1005.2 and 142.4 µmol $h^{-1}$ $g^{-1}$, respectively. From Fig. 4c and d, $TiO_2$ NBs show a medium activity for the photocatalytic water oxidation, giving an average $O_2$ production rate of 145.0 µmol $h^{-1}$ $g^{-1}$, while $Co_3O_4$ could be a promising candidate, exhibiting the average $O_2$ evolution rate of 309.6 µmol·$h^{-1}$·$g^{-1}$. The coupling of $Co_3O_4$ QDs and $TiO_2$ NBs with a $Co_3O_4/TiO_2$ molar ratio of 0.04 facilitates the reaction, and the average $O_2$ evolution rate is further

elevated to 473.8 µmol $h^{-1}$ $g^{-1}$. The average $O_2$ production rates for $Co_3O_4/TiO_2$-0.02 and $Co_3O_4/TiO_2$-0.06 are 237.5 and 39.1 µmol $h^{-1}$ $g^{-1}$, respectively.

The overall photocatalytic water-splitting performances of $Co_3O_4/$ $TiO_2$-0.04, $TiO_2$ NBs and $Co_3O_4$ were further measured in neutral water without any sacrificial reagent or noble metal under the simulated solar light. The typical time course of simultaneous evolution of $H_2$ and $O_2$ gases on the three catalysts are presented in Fig. 5. $Co_3O_4/TiO_2$-0.04 and $TiO_2$ NBs exhibit the constant rates of $H_2$ and $O_2$ at an expected molar ratio of ~2:1 for the overall water splitting, interpreting that the evolved $O_2$ is mostly originated from water oxidation. It is also suggested that the photo-generated electrons and holes are well separated and equally consumed by the water splitting reaction. The $H_2$ generation rate on $Co_3O_4/TiO_2$-0.04 is promoted to 41.8 µmol $h^{-1}$ $g^{-1}$ from 24.2 µmol $h^{-1}$ $g^{-1}$ on $TiO_2$ NBs, illustrating that the decoration of $Co_3O_4$ QDs on $TiO_2$ NBs improves the separation and transfer of photo-generated carries successfully. For pure $Co_3O_4$ catalyst, only $O_2$ is produced with a reaction rate of 10.0 µmol·$h^{-1}$·$g^{-1}$, while $H_2$ could not be detected. This phenomenon may be related to the nature of the surface redox active sites on $Co_3O_4$ for $H_2$ and $O_2$ evolutions, and the formed photo-generated electrons may be consumed by the surface species of $Co_3O_4$. Additionally, the stability of the $Co_3O_4/TiO_2$-0.04 in the photocatalytic overall water splitting was tested in recycling investigations as seen in Fig. 5d. After each run the reaction system was evacuated. From Fig. 5, the photocatalytic activity of $Co_3O_4/TiO_2$-0.04 displayed no noticeable decrease in the reaction period running for 3 times.

### 3.3. Photochemical properties of catalysts

The charge transfer properties of photocatalysts were measured via electrochemical independence spectroscopy (EIS) measurements. As displayed in Fig. 6a, the electronic resistance of $Co_3O_4/TiO_2$-0.04 is greatly reduced than that of $TiO_2$ NBs as indicated by the smaller impedance arc radius, which is further decreased due to the light excitation. Herein, it is suggested that the loading of $Co_3O_4$ QDs, which is sensitive to the light irradiation, favors to increase the carrier density and enhances the diffusion of electrons with high mobility [42,43]. Fig. 6b displays the time-resolved photoresponse of the three catalysts to reflect the photo-to-current conversion efficiency. $Co_3O_4/TiO_2$-0.04 exhibits a photocurrent density of ~0.50 µA $cm^{-2}$ under the irradiation of simulated solar light, significantly higher than that of $TiO_2$ NBs (~0.32 µA $cm^{-2}$) and $Co_3O_4$ (~0.25 µA $cm^{-2}$) samples.

### 3.4. Optical property and energy band structure of catalysts

UV-vis absorption spectra of $TiO_2$ NBs, $Co_3O_4$ and $Co_3O_4/TiO_2$-0.04 are presented in Fig. 7a. The absorption edge of $TiO_2$ is at about 340 nm, exhibiting the weak photo-response to the visible light. In the case of pure $Co_3O_4$, a broad absorption spectrum is observed, and the loading of $Co_3O_4$ QDs on $TiO_2$ NBs leads to increased absorption in the
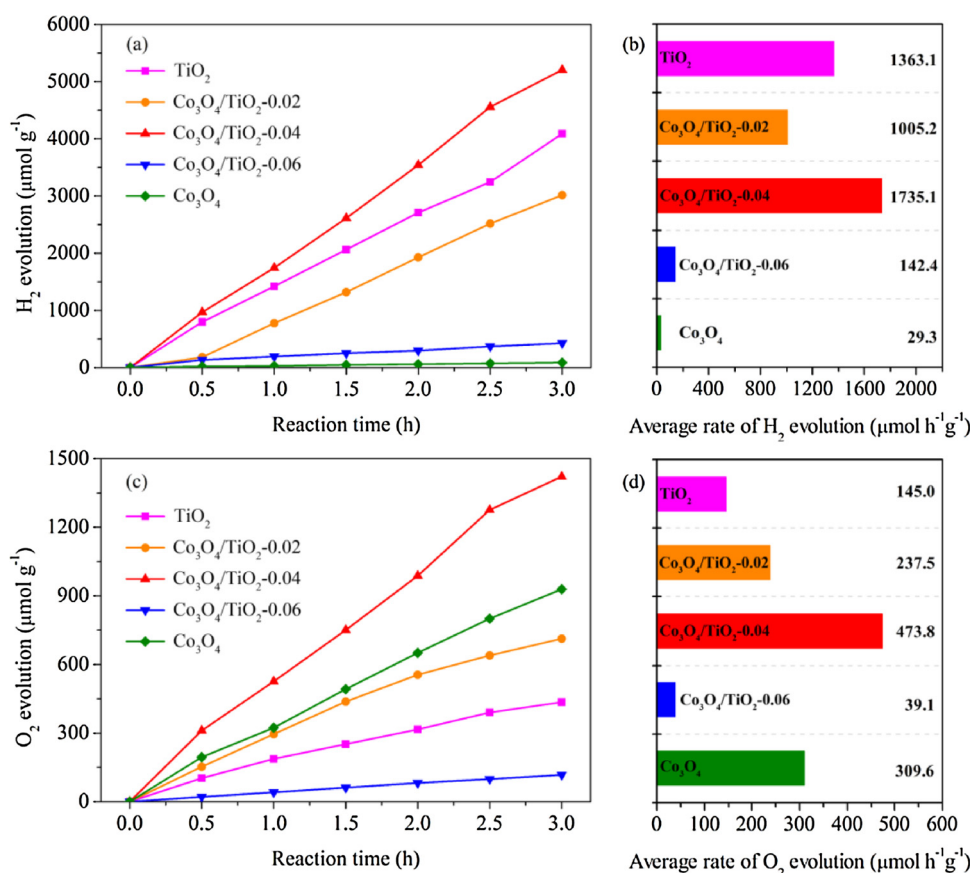
**Fig. 4.** Performance of $TiO_2$, $Co_3O_4$ and various $Co_3O_4/TiO_2$ catalysts in the photocatalytic half reactions of water splitting: (a, b) hydrogen evolution and (c, d) oxygen evolution.

visible light range. The band gap of the catalysts can be estimated from Tauc plots by $(\alpha h\nu) = A(h\nu - E_g)^{1/2}$, in which $\alpha$, $\nu$, $A$ and $E_g$ are the absorption coefficient, light frequency, proportionality constant, and band gap, respectively. As shown in Fig. 7b, the band gaps of $TiO_2$ NB, $Co_3O_4$ and $Co_3O_4/TiO_2$-0.04 were determined to be 3.83, 1.70 and 3.07 eV, respectively, demonstrating the evident enhancement of photo-response ability on a heterojunction system.

The PL emission spectra can reflect the effectiveness of the charge trapping, immigration and transfer behaviors of the photoexcited electron-hole pairs in semiconductors. Fig. 8 presents the PL emission ($\lambda_{exc}$ = 325 nm) spectra of the as-prepared $TiO_2$, $Co_3O_4$ and $Co_3O_4/TiO_2$-0.04 samples. For the $TiO_2$ and $Co_3O_4/TiO_2$-0.04 catalysts, the strong peak around 412 nm could be attributed to the free excitations at the band edge of $TiO_2$, while the peaks at 468 and 546 nm are assigned to the deep level defects and the oxygen vacancies, respectively [44,45]. Moreover, the shoulder bands at 450 and 493 nm are also reported as the oxygen vacancies [46]. The defect level indicates the radiative recombination, and the oxygen vacancies trap the photo-emission electrons from the conduction band via non radiative transition, both of which result in the increase of PL intensity [44]. For the $Co_3O_4$ sample, the apparent emission peak appears at 654 nm, and it could be attributed to the structural defects, caused by the cobalt ions occupying interstitial positions. This feature is also detected on the $Co_3O_4/TiO_2$-0.04 sample, but the intensity is much weakened. It is well known that the lower PL intensity suggests the higher separation efficiency of the charge carriers and the less recombination of the electrons and holes [23,45,47]. Herein, the evidently decreased PL intensity of the $Co_3O_4/TiO_2$-0.04 sample illustrates its enhanced photocatalysis from the view of the separation and recombination behaviors of the photo-generated carries.

The change in valence band electronic structure of $TiO_2$ NBs caused

by the loading of $Co_3O_4$ QDs was investigated by VB-XPS measurements. From Fig. 9a, the valence band maximum (VBM) values of $Co_3O_4$, $TiO_2$ NBs and the as-prepared $Co_3O_4/TiO_2$-0.04 hybrid are 0.60, 2.85, and 2.35 eV, respectively, corresponding to their Fermi levels ($E_f$). Compared with $TiO_2$ NBs, VB-XPS spectra of $Co_3O_4/TiO_2$-0.04 exhibit a more remarkable VB tail state, suggesting the possible generation of additional diffusive electronic states above the VB edge, which could be induced by the generation of heterojunctions between $TiO_2$ and $Co_3O_4$ QDs [48,49]. UPS is used to determine the work function ($\Phi$) of the catalysts, to further clarify the decoration effect of $Co_3O_4$ QDs on the energy band. The $\Phi$ values of $Co_3O_4$, $TiO_2$ and $Co_3O_4/TiO_2$-0.04 hybrid are 5.76, 4.94 and 5.12 eV, respectively, representing the differences between the vacuum (0 eV) and $E_f$ energy levels of the catalysts.

Combining the band gap obtained from DRS profiles, VB-XPS and UPS results, the locations of $E_f$, valance band (VB) and conductive band (CB) of various catalysts are presented in Fig. 10a. From the viewpoint of band structure, the CB position of pure $Co_3O_4$ is slightly lower than the redox potential of $H^+/H_2$ (0 V *vs.* NHE), while the VB position is suitable for $O_2$ evolution (potential of $O_2/H_2O$ is 1.23 V *vs.* NHE), which explains the performance of $Co_3O_4$ in the overall water splitting for only oxygen production. From Fig. 10a the band structures of $TiO_2$ NBs and $Co_3O_4/TiO_2$-0.04 hybrid match well with the reaction of overall water splitting. Compared with $TiO_2$ NBs, the work function of $Co_3O_4/TiO_2$-0.04 is increased due to the loading of $Co_3O_4$ QDs, illustrating the spontaneous transfer of the electrons from $TiO_2$ to $Co_3O_4$ QDs, which leads to the shifting of the Fermi level to more negative potential, while the photo-excited holes remain in $TiO_2$ [50,51]. Herein, it is suggested that the formation of $Co_3O_4$ QDs/$TiO_2$ heterojunctions promotes the transfer of photo-excited electrons and holes, and benefits to inhibit their recombination. Moreover, the small size of $Co_3O_4$ QDs as well as their high surface area offer a shorter charge transfer pathway, further
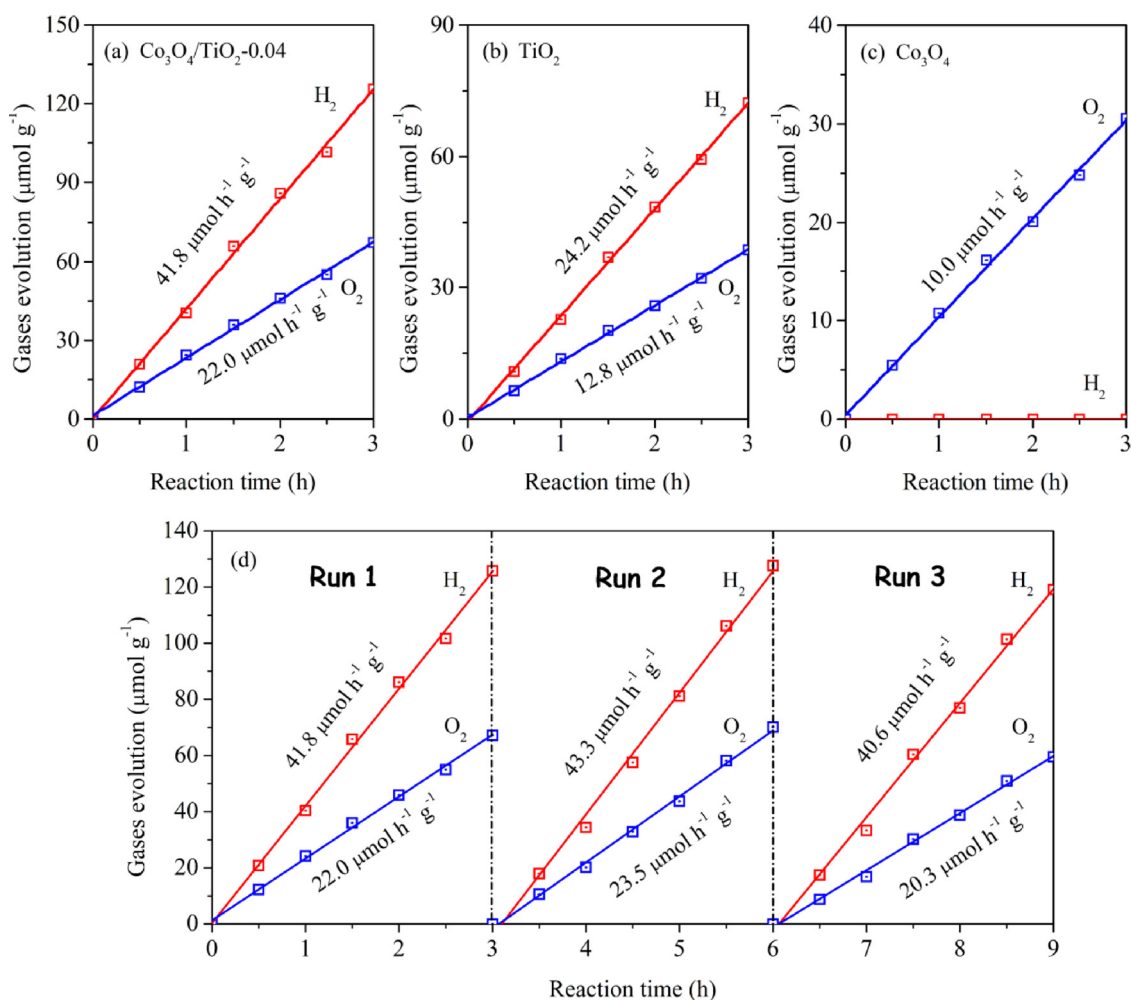
**Fig. 5.** Typical time course of $H_2$ and $O_2$ production from photocatalytic overall water splitting by the as-prepared $Co_3O_4/TiO_2$-0.04 (a), $TiO_2$ NBs (b) and $Co_3O_4$ (c) catalysts, and the recycling tests of the $Co_3O_4/TiO_2$-0.04 sample for photocatalytic overall water splitting (d).

fastening the trapping of the electrons from $TiO_2$. Then it is likely that the electrons are readily to be accumulated on the surface of $Co_3O_4$ QDs to participate in the hydrogen evolution, and the holes in $TiO_2$ lead to the water oxidation, as the reaction mechanism of $Co_3O_4$ QDs/$TiO_2$ hybrid for overall water splitting is displayed in Fig. 10b.

## 4. Conclusions

In summary, a $Co_3O_4$ QDs/$TiO_2$ NBs hybrid with $Co_3O_4/TiO_2$ ratio of 0.04 was fabricated for the overall water splitting without any sacrificial agent and noble metal, by a facile hydrothermal method. The $H_2$ and $O_2$ production rates on the as-prepared $Co_3O_4$ QDs/$TiO_2$ hybrid were 41.8 and 22.0 $\mu mol\, h^{-1}\, g^{-1}$, respectively, under the simulated solar light. Due to the decoration of $Co_3O_4$ QDs, the band gap of $Co_3O_4$
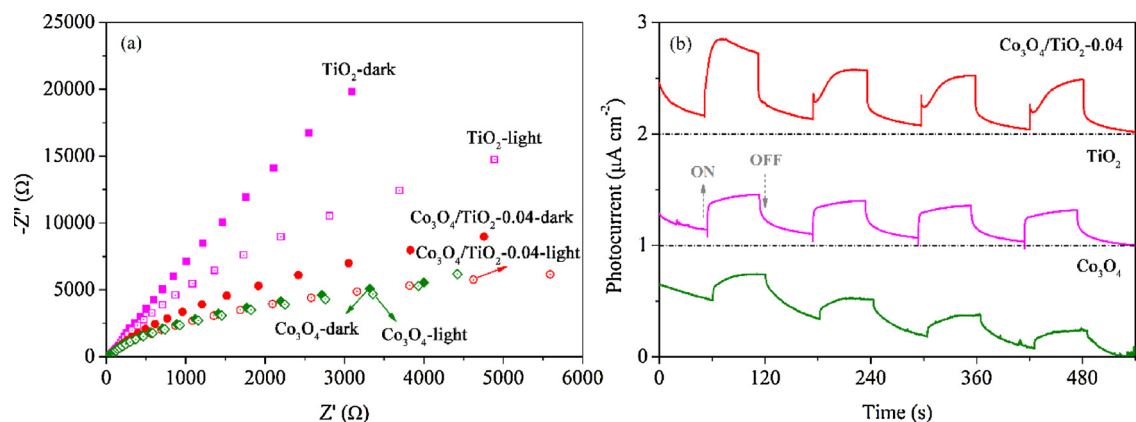


**Fig. 6.** EIS spectra of the as-prepared $TiO_2$ NBs, $Co_3O_4$ and $Co_3O_4/TiO_2$-0.04 catalysts (a), and Time-resolved photoresponse of the catalysts under irradiation at + 0.6 V versus saturated calomel electrode (b).
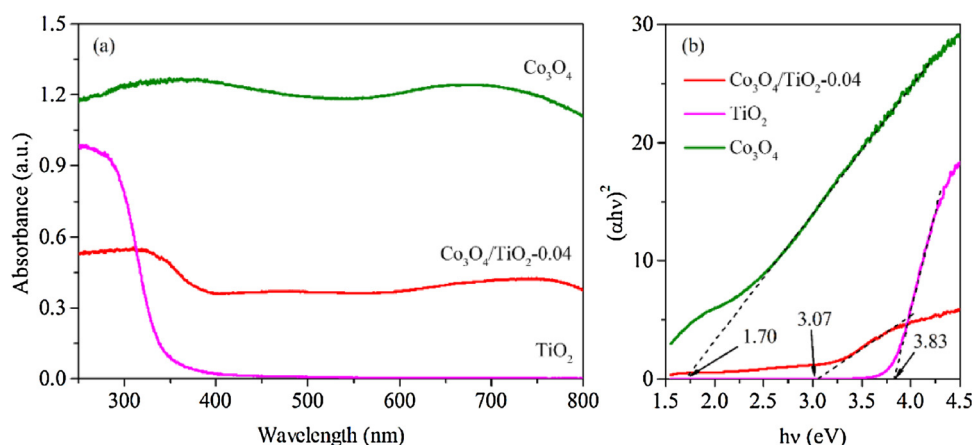
**Fig. 7.** DRS spectra (a) and the corresponding Tauc plots (b) of the as-prepared $TiO_2$ NBs, $Co_3O_4$ and $Co_3O_4/TiO_2$-0.04 samples.
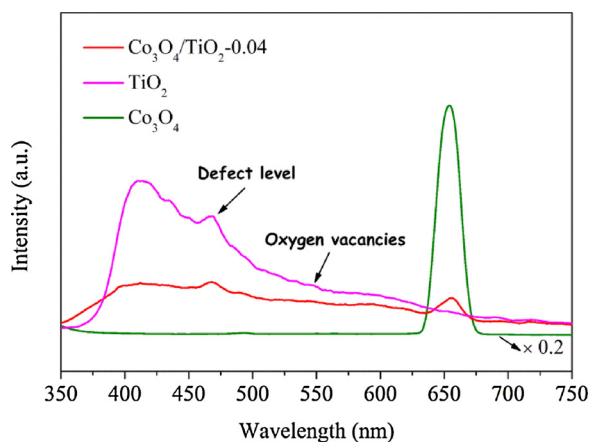


**Fig. 8.** Photoluminescence spectra of the as-prepared $TiO_2$ NBs, $Co_3O_4$ and $Co_3O_4/TiO_2$-0.04 samples.

QDs/$TiO_2$ hybrid was narrowed to enhance the light response of the catalyst and the charge separation significantly. More importantly, the coupling of $Co_3O_4$ QDs and $TiO_2$ led to the realignment of band structure to fit the reaction of overall water splitting. It is believed that the size effect of $Co_3O_4$ QDs and the generation of $Co_3O_4$ QDs/$TiO_2$ heterojunction favored the transfer and accumulation of photo-generated electrons on $Co_3O_4$ QDs, to participate into the reaction of $H_2$ evolution, and the recombination of photo-generation charge carries was inhibited at the meantime. The proposed mechanism and the enhanced efficiency of $Co_3O_4$ QDs/$TiO_2$ heterojunction photocatalyst provides a promising opportunity for further development of based on $TiO_2$ materials toward solar water splitting.

## Acknowledgements
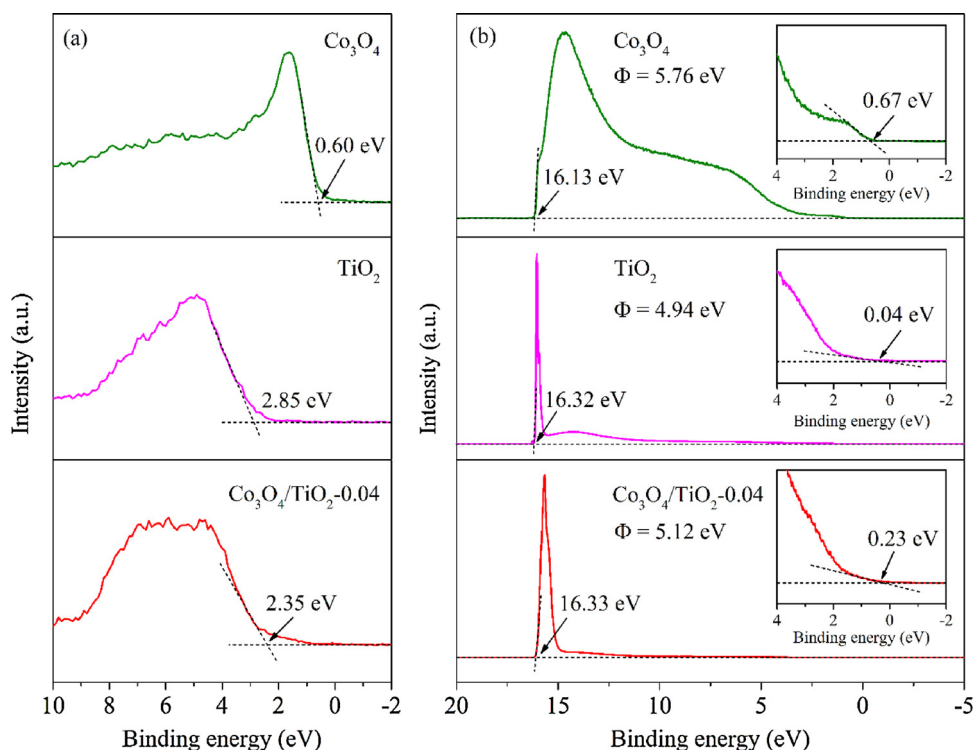
**Fig. 9.** VB-XPS (a) and UPS (b) spectra of the as-prepared $TiO_2$ NBs, $Co_3O_4$ and $Co_3O_4/TiO_2$-0.04, inset: detailed spectra of secondary electron cutoff region.
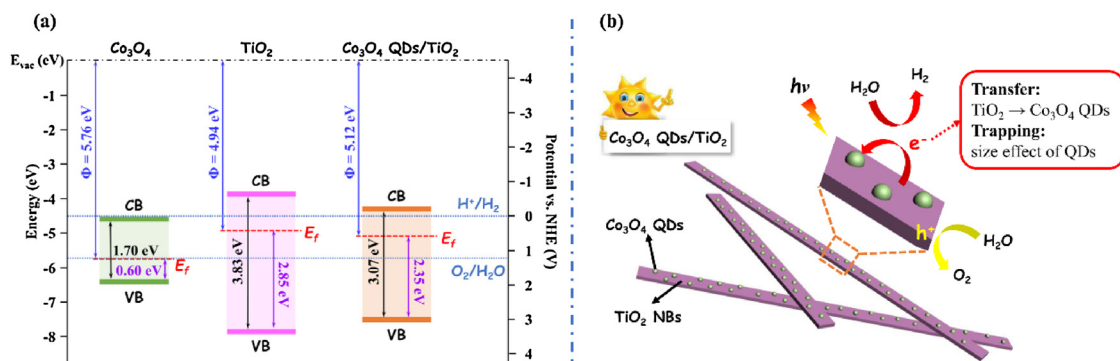
**Fig. 10.** Band structure of the as-prepared TiO₂ NBs, Co₃O₄ and Co₃O₄/TiO₂-0.04 samples (a), and the proposed mechanism for the enhanced activity of Co₃O₄/TiO₂-0.04 in the photocatalytic overall water splitting (b).

## Appendix A. Supplementary data

Supplementary material related to this article can be found, in the online version, at doi: https://doi.org/10.1016/j.apcatb.2018.05.042.

## References

[1] Q. Han, B. Wang, J. Gao, Z. Cheng, Y. Zhao, Z. Zhang, L. Qu, ACS Nano 10 (2016) 2745–2751.
[2] K. Maeda, N. Murakami, T. Ohno, J. Phys. Chem. C 118 (2014) 9093–9100.
[3] Q. Zhang, Z. Li, S. Wang, R. Li, X. Zhang, Z. Liang, H. Han, S. Liao, C. Li, ACS Catal. 6 (2016) 2182–2191.
[4] J. Ke, J. Liu, H. Sun, H. Zhang, X. Duan, P. Liang, X. Li, M.O. Tade, S. Liu, S. Wang, Appl. Catal. B: Environ. 200 (2017) 47–55.
[5] H. Liu, R. More, H. Grundmann, C. Cui, R. Erni, G.R. Patzke, J. Am. Chem. Soc. 138 (2016) 1527–1535.
[6] N. Li, S. Tang, Y. Rao, J. Qi, P. Wang, Y. Jiang, H. Huang, J. Gu, D. Yuan, Electrochim. Acta 270 (2018) 330–338.
[7] H. Xu, J. Yi, X. She, Q. Liu, L. Song, S. Chen, Y. Yang, Y. Song, R. Vajtai, J. Lou, H. Li, S. Yuan, J. Wu, P.M. Ajayan, Appl. Catal. B: Environ. 220 (2018) 379–385.
[8] H. Zhang, J. Cai, Y. Wang, M. Wu, M. Meng, Y. Tian, X. Li, J. Zhang, L. Zheng, Z. Jiang, J. Gong, Appl. Catal. B: Environ. 220 (2018) 126–136.
[9] K. Maeda, K. Domen, J. Phys. Chem. Lett. (2010) 2655–2661.
[10] Y. Zhang, L. Han, C. Wang, W. Wang, T. Ling, J. Yang, C. Dong, F. Lin, X. Du, ACS Catal. 7 (2017) 1470–1477.
[11] J. Ke, H. Zhou, J. Liu, X. Duan, H. Zhang, S. Liu, S. Wang, J. Colloid Interface Sci. 514 (2018) 576–583.
[12] W. Liu, L. Cao, W. Cheng, Y. Cao, X. Liu, W. Zhang, X. Mou, L. Jin, X. Zheng, W. Che, Q. Liu, T. Yao, S. Wei, Angew. Chem. Int. Ed. 129 (2017) 9440–9445.
[13] M. Zhu, Z. Sun, M. Fujitsuka, T. Majima, Angew. Chem. In. Ed. 57 (2018) 1–6.
[14] S. Tan, Z. Xing, J. Zhang, Z. Li, X. Wu, J. Cui, J. Kuang, Q. Zhu, W. Zhou, J. Catal. 357 (2018) 90–99.
[15] Q. Lang, Y. Chen, T. Huang, L. Yang, S. Zhong, L. Wu, J. Chen, S. Bai, Appl. Catal. B: Environ. 220 (2018) 182–190.
[16] S. Wang, X. Luo, X. Zhou, Y. Zhu, X. Chi, W. Chen, K. Wu, Z. Liu, S. Quek, G. Xu, J. Am. Chem. Soc. 139 (2017) 15414–15419.
[17] S. Tang, D. Yuan, Y. Rao, N. Li, J. Qi, T. Cheng, Z. Sun, J. Gu, H. Huang, Chem. Eng. J. 337 (2018) 446–454.
[18] J. Ke, X. Duan, S. Luo, H. Zhang, H. Sun, J. Liu, M. Tade, S. Wang, Chem. Eng. J. 313 (2017) 1447–1453.
[19] X. Dong, W. Zhang, Y. Sun, J. Li, W. Cen, Z. Cui, H. Huang, F. Dong, J. Catal. 357 (2018) 41–50.
[20] S.-i. Fujita, H. Kawamori, D. Honda, H. Yoshida, M. Arai, Appl. Catal. B: Environ. 181 (2016) 818–824.
[21] N. Shi, W. Cheng, H. Zhou, T. Fan, M. Niederberger, Chem. Commun. 51 (2015) 1338–1340.
[22] R. Tang, S. Zhou, Z. Yuan, L. Yin, Adv. Funct. Mater. 27 (2017) 1701102–1701113.
[23] W. Wei, X. Liu, S. Cui, J. Liu, RSC Adv. 7 (2017) 25650–25656.
[24] A. Meng, J. Zhang, D. Xu, B. Cheng, J. Yu, Appl. Catal. B: Environ. 198 (2016) 286–294.
[25] K. Maeda, K. Ishimaki, M. Okazaki, T. Kanazawa, D. Lu, S. Nozawa, H. Kato, M. Kakihana, ACS Appl. Mater. Interfaces 9 (2017) 6114–6122.
[26] J. Ye, K. Ni, J. Liu, G. Chen, M. Ikram, Y. Zhu, ChemCatChem 9 (2018) 259–265.
[27] S. Lian, M.S. Kodaimati, E.A. Weiss, ACS Nano 12 (2018) 568–575.
[28] Z. Zheng, F. Zhuge, Y. Wang, J. Zhang, L. Gan, X. Zhou, H. Li, T. Zhai, Adv. Funct. Mater. 27 (2017) 1703115–1703126.
[29] W. Hong, Y. Zhou, C. Lv, Z. Han, G. Chen, ACS Sustain. Chem. Eng. 6 (2018) 889–896.
[30] D. Zeng, W. Xu, W.-J. Ong, J. Xu, H. Ren, Y. Chen, H. Zheng, D.-L. Peng, Appl. Catal. B: Environ. 221 (2018) 47–55.
[31] H. Zhang, W. Tian, L. Zhou, H. Sun, M. Tade, S. Wang, Appl. Catal. B: Environmental 223 (2018) 2–9.
[32] M. Ye, Z. Zhao, Z. Hu, L. Liu, H. Ji, Z. Shen, T. Ma, Angew. Chem. Int. Ed. 56 (2017) 1–6.
[33] H.-F. Wang, L.-Y. Chen, W.-N. Su, J.-C. Chung, B.-J. Hwang, J. Phys. Chem. C 114 (2010) 3185–3189.
[34] C. Xu, H. Geng, R. Bennett, D.A. Clayton, S. Pan, J. Phys. Chem. C 117 (2013) 1849–1856.
[35] C. Wang, P. Shi, X. Cai, Q. Xu, X. Zhou, X. Zhou, D. Yang, J. Fan, Y. Min, H. Ge, W. Yao, J. Phys. Chem. C 120 (2015) 336–344.
[36] K.P. Reddy, R. Jain, M.K. Ghosalya, C.S. Gopinath, J. Phys. Chem. C 121 (2017) 21472–21481.
[37] H. Huang, X. Li, J. Wang, F. Dong, P.K. Chu, T. Zhang, Y. Zhang, ACS Catal. 5 (2015) 4094–4103.
[38] F. Zhang, X. Li, Q. Zhao, A. Chen, J. Phys. Chem. C 120 (2016) 19113–19123.
[39] J. Liu, Y. Li, J. Ke, S. Wang, L. Wang, H. Xiao, Appl. Catal. B: Environ. 224 (2018) 705–714.
[40] J. Liu, X. Li, R. Li, Q. Zhao, J. Ke, H. Xiao, L. Wang, S. Liu, M. Tadé, S. Wang, Appl. Catal. A: Gen. 549 (2018) 289–301.
[41] J. Liu, X. Li, Q. Zhao, J. Ke, H. Xiao, X. Lv, S. Liu, M. Tadé, S. Wang, Appl. Catal. B: Environ. 200 (2017) 297–308.
[42] B. Huang, W. Yang, Y. Wen, B. Shan, R. Chen, ACS Appl. Mater. Interfaces 7 (2015) 422–431.
[43] G. Zhang, Q. Ji, Z. Wu, G. Wang, H. Liu, J. Qu, J. Li, Adv. Funct. Mater. 28 (2018) 1706462.
[44] A.C. Pradhan, T. Uyar, ACS Appl. Mater. Interfaces 9 (2017) 35757–35774.
[45] T. Li, X. Li, Q. Zhao, Y. Shi, W. Teng, Appl. Catal. B: Environ. 156-157 (2014) 362–370.
[46] Q. Chen, S. Wu, Y. Xin, Chem. Eng. J. 302 (2016) 377–387.
[47] W.-J. Ong, L.K. Putri, L.-L. Tan, S.-P. Chai, S.-T. Yong, Appl. Catal. B: Environ. 180 (2016) 530–543.
[48] J. Liu, J. Ke, D. Li, H. Sun, P. Liang, X. Duan, W. Tian, M.O. Tadé, S. Liu, S. Wang, ACS Appl. Mater. Interfaces 9 (2017) 11678–11688.
[49] J. Liu, L. Han, N. An, L. Xing, H. Ma, L. Cheng, J. Yang, Q. Zhang, Appl. Catal. B: Environ. 202 (2014) 642–652.
[50] A. Migani, L. Blancafort, J. Am. Chem. Soc. 138 (2016) 16165–16173.
[51] I. Shown, H.C. Hsu, Y.C. Chang, C.H. Lin, P.K. Roy, A. Ganguly, C.H. Wang, J.K. Chang, C.I. Wu, L.C. Chen, K.H. Chen, Nano Lett. 14 (2014) 6097–6103.